**Astronomy
&
Astrophysics**

Precise radial velocities of giant stars

VIII. Testing for the presence of planets with CRIRES infrared radial velocities[*],[**]

Trifon Trifonov[1,2], Sabine Reffert[1], Mathias Zechmeister[3], Ansgar Reiners[3], and Andreas Quirrenbach[1]

[1] Landessternwarte, Zentrum für Astronomie der Universität Heidelberg, Königstuhl 12, 69117 Heidelberg, Germany
    e-mail: t.trifonov@lsw.uni-heidelberg.de
[2] Department of Earth Sciences, The University of Hong Kong, Pokfulam Road, Hong Kong
[3] Institut für Astrophysik, Georg-August-Universitä, Friedrich-Hund-Platz 1, 37077 Göttingen, Germany

ABSTRACT

Context. We have been monitoring 373 very bright ($V \leq 6$ mag) G and K giants with high precision optical Doppler spectroscopy for more than a decade at Lick Observatory. Our goal was to discover planetary companions around those stars and to better understand planet formation and evolution around intermediate-mass stars. However, in principle, long-term, g-mode nonradial stellar pulsations or rotating stellar features, such as spots, could effectively mimic a planetary signal in the radial velocity data.
Aims. Our goal is to compare optical and infrared radial velocities for those stars with periodic radial velocity patterns and to test for consistency of their fitted radial velocity semiamplitudes. Thereby, we distinguish processes intrinsic to the star from orbiting companions as reason for the radial velocity periodicity observed in the optical.
Methods. Stellar spectra with high spectral resolution have been taken in the H-band with the CRIRES near-infrared spectrograph at ESO's VLT for 20 stars of our Lick survey. Radial velocities are derived using many deep and stable telluric CO_2 lines for precise wavelength calibration.
Results. We find that the optical and near-infrared radial velocities of the giant stars in our sample are consistent. We present detailed results for eight stars in our sample previously reported to have planets or brown dwarf companions. All eight stars passed the infrared test.
Conclusions. We conclude that the planet hypothesis provides the best explanation for the periodic radial velocity patterns observed for these giant stars.

Key words. planetary systems – instrumentation: spectrographs – techniques: radial velocities – methods: observational

1. Introduction

By June 2015, the number of confirmed substellar companions discovered with the Doppler technique has reached ~600[1]. This number constitutes ~30% of the total number of planets discovered using all planet search methods. In addition, many more extrasolar planets, in particular those discovered with the transiting method, have been confirmed with Doppler spectroscopy. This shows that the precise radial velocity (RV) method still remains one of the most valuable extrasolar planet search tools to date.

Ultra stable échelle spectrographs, such as HARPS (Mayor et al. 2003), have already reached sub-m s^{-1} precision and potentially allow astronomers to search for Earth mass planets. The Doppler technique, however, can suffer from false positive detections due to RV variations intrinsic to a star. In addition to short period p-mode pulsations (Barban et al. 2004; Zechmeister et al. 2008), which are excited by convection and seen as stellar RV scatter, stellar surface spots or even nonradial gravitational

g-mode pulsations can potentially cause line shape deformations, which can be misinterpreted as velocity shifts.

So far, more than 60 substellar companions have been detected around evolved G and K giant stars using the Doppler method. Some of these stars have RV signals clearly consistent with highly eccentric substellar companions that cannot be mistaken for stellar activity (e.g., Frink et al. 2002; Moutou et al. 2011; Sato et al. 2013), but for others an alternative explanation of the data cannot be excluded despite their periodic RV signals. While long-term g-mode pulsations are rather unlikely to be excited in the large convective layers in these evolved stars, temperature spots on the other hand could effectively mimic a planet (e.g., Hatzes & Cochran 2000). As K giants are inflated stars compared to their main-sequence progenitors, their rotational period can be of the order of hundreds of days. Therefore, in case of spot(s) on the stellar surface, the line profile variations can lead to RV variations with long periods and semiamplitudes significantly surpassing the intrinsic stellar jitter that can be easily mistaken for a planet.

Detailed studies of spectral line profile bisectors have often been used to support the companion hypothesis. This method requires very high resolution spectra, however, and a stable instrumental profile, and the absence of variations in the spectral line shape is a necessary condition, but is not sufficient to prove the existence of a substellar companion definitively.

Measuring RV signals in the near-infrared (near-IR) is another promising test that can be performed. The contrast ratio between the star's surface blackbody intensity and that of a cooler spot is much larger in the optical than in the IR domain. In case of spots, line shape deformations in the IR data must have a much smaller amplitude (Desort et al. 2007; Reiners et al. 2010). We can also expect different RV amplitudes in the two domains in case of nonradial g-mode pulsations, while this test should yield no difference in the optical and near-IR RVs in case of a planet.

A prominent example for the discussion of spot-induced RVs is the young star TW Hya; Setiawan et al. (2008) found periodic RV variations, but no indication of line bisector variations and concluded that the star is orbited by a planet. Later, Huélamo et al. (2008) observed TW Hya at infrared wavelengths but could not find RV variations consistent with the Keplerian solution from optical measurements. Huélamo et al. (2008) concluded that no planet orbits TW Hya.

High precision RVs derived from the infrared wavelength regime can form a rather critical test for planet confirmation. This test is valid mostly for active stars for which other viable explanations for periodic RVs, such as spots or pulsations, cannot be excluded by any other means, such as giant stars in particular.

An obvious choice for this test is the ESO pre-dispersed CRyogenic InfraRed Echelle Spectrograph (CRIRES), mounted at the Nasmyth focus B of the 8 m VLT UT1 (Kaeufl et al. 2004). Several studies demonstrated that RV measurements with precision between 10 and 35 m s^{-1} are possible with CRIRES. Seifahrt & Käufl (2008) reached a precision of $\approx$35 m s^{-1} for CRIRES RVs, using the N$_2$O gas cell for calibration. Huélamo et al. (2008) and Figueira et al. (2010) showed that a Doppler precision of $\approx$10 m s^{-1} can be achieved when using telluric CO$_2$ lines in the H-band as wavelength reference.

We present our CRIRES near-infrared Doppler results for 20 evolved G8-K4 III giant stars. All selected targets in this study have periodic RVs as derived from optical spectra, and are thus potential planet hosts. They constitute a small subsample of our K giant planet search sample in the optical (Frink et al. 2001; Reffert et al. 2015).

In Sect. 2 we briefly introduce the background of this program. Section 3 describes our observational setup with CRIRES. In Sect. 4 we explain in detail the data reduction and analysis process with our CRIRES pipeline. Our methods of extracting the precise RVs are given in Sect. 5, and in Sect. 6 we discuss the consistency between optical and IR data. In Sect. 7 we discuss our results, and we provide a summary in Sect. 8.

2. The K giant sample

Our Doppler survey started in 1999 at Lick Observatory using the Hamilton spectrograph in conjunction with an iodine cell (Marcy & Butler 1992; Butler et al. 1996). The initial goal of our program and the star selection criteria are described in Frink et al. (2001). Briefly, we regularly observed 373 very bright ($V \leq 6$ mag) and photometrically constant G and K giants selected from the Hipparcos Catalog. The objective of our program is to investigate and understand giant planet occurrence and evolution around intermediate-mass stars.

The first planet from our program was discovered around the K giant star ι Dra (Frink et al. 2002). The highly eccentric Keplerian reflex motion of ι Dra seen in the Lick data leaves no doubt on the planet's existence. Therefore, ι Dra b became the first confirmed extrasolar planet around a giant star and encouraged more scientists to search for extrasolar planets around

evolved stars with the Doppler method. As a result, to date more than 60 planets[2] have been discovered around giants, and their number is constantly growing.

Planet occurrence statistics and more results from our Lick survey are given in Reffert et al. (2015). We distinguish between planets and planet candidates among the companions, depending on how persistent the RV signal is over many cycles, and how large the RV amplitude is compared to the intrinsic RV jitter caused by short-term radial pulsations.

A subsample of 20 stars with planets and planet candidates from our survey is of particular interest, and are studied further here. All these stars display either one or two clear periodicities in their RVs, consistent with one or two orbiting substellar companions with minimum masses ranging between a few Jupiter masses and a low-mass brown dwarf. If stellar spots were responsible for the obtained Doppler velocities, they would correspond to photometric variability (Hatzes 2002). Precise photometry from Hipparcos shows that our sample is photometrically stable down to 3 mmag, and thus there are no indications for any intrinsic features to be related to a Doppler signal (Reffert et al. 2015). Nevertheless, since we cannot fully exclude long-period pulsations (g-mode or of unknown nature), we have observed our subsample of 20 stars with CRIRES over four semesters in an attempt to provide more evidence in favor of the companion hypothesis. Stars are listed in Table 1, including their Hipparcos and HD number, apparent magnitude in V and H bands, as well as basic physical parameters, such as stellar mass M, radius R, and luminosity L as given in Reffert et al. (2015). Some planetary systems from the subsample have already been published: HIP 37826 (Reffert et al. 2006), HIP 88048 (Quirrenbach et al. 2011), HIP 34693 and HIP 114855 (Mitchell et al. 2013), and HIP 5364 (Trifonov et al. 2014). Others have been discovered independently: HIP 37826 (Hatzes et al. 2006), HIP 20889 (Sato et al. 2007), HIP 60202 (Liu et al. 2008), and HIP 31592 (Wittenmyer et al. 2011). Publication of the remaining stars with confirmed planets is in preparation.

3. Observational setup

The ESO's CRIRES instrument is a temperature stabilized near-infrared spectrograph with a maximum resolution of $R \approx 100\,000$ when used with a 0.2$''$ slit. Despite a broad accessible wavelength range from 950 to 5200 nm (J, H, K, L, and M infrared bands), the available wavelength coverage per single observation in this predispersed échelle spectrograph is much smaller than in optical cross-dispersed échelle spectrographs and currently limited to one spectral order[3]. A particular wavelength setting can be selected for each observation, with a free spectral range on the order of $20-200$ nm, depending on the spectral order and the dispersion for that setting. The spectrum is imaged by a mosaic of four Aladdin III detectors, forming an effective 4096×512 pixel array (with a gap of $\sim$280 px between the detectors). This arrangement is somewhat problematic because a precise wavelength solution must be obtained separately for each detector. The standard CRIRES pipeline recipes offer in principle this kind of calibration, but at a level of RV precision far below that required for the Doppler detection of planets.

---

[3] Currently, CRIRES is removed from UT1 for an upgrade and is expected to be operational again in 2017 under the name CRIRES+. The new instrument is expected to cover simultaneously a wavelength range about ten times larger than the original (Dorn et al. 2014).

Table 1. List of observed stars.

HIP number	HD number	Sp.type[α]	M^{β} [$M_{\odot}$]	R^{β} [$R_{\odot}$]	L^{β} [$L_{\odot}$]	V^{α} [mag]	H^{γ} [mag]	N obs.
5364	6805	K2 III	1.7 ± 0.1	14.3 ± 0.2	71.1 ± 1.1	3.46	1.0	9
19011	25723	K1 III	2.1 ± 0.3	13.9 ± 0.6	89.5 ± 7.2	5.62	3.1	6
20889	28305	K0 III	2.4 ± 0.2	13.1 ± 0.2	85.3 ± 2.7	3.53	1.3	8
23015	31398	K3 II	4.5 ± 0.6	126.3 ± 12.6	3752.8 ± 675.1	2.69	−0.7	6
31592	47205	K1 III	1.4 ± 0.2	5.1 ± 0.3	12.0 ± 0.6	3.95	1.7	9
34693	54719	K2 III	2.3 ± 0.3	36.8 ± 0.7	238.4 ± 11.4	4.41	1.8	8
36616	59686	K2 III	1.9 ± 0.2	13.2 ± 0.3	73.3 ± 3.4	5.45	3.1	8
37826	62509	K0 III	2.3 ± 0.2	8.7 ± 0.3	39.8 ± 0.6	1.16	−0.8	8
38253	63752	K3 III	2.0 ± 0.5	69.4 ± 11.3	1169.2 ± 379.8	5.60	2.5	8
39177	65759	K3 III	2.7 ± 0.6	20.4 ± 1.4	473.2 ± 134.2	5.60	2.9	7
60202	107383	G8 III	2.2 ± 0.3	15.6 ± 0.4	112.0 ± 4.6	4.72	2.5	7
73133	131918	K4 III	1.2 ± 0.1	44.0 ± 2.1	408.2 ± 39.8	5.48	2.3	6
74732	135534	K2 III	1.5 ± 0.2	26.5 ± 1.1	200.1 ± 16.0	5.52	2.7	7
79540	145897	K3 III	1.1 ± 0.2	26.8 ± 0.8	190.9 ± 10.5	5.24	2.3	8
80693	148513	K4 III	1.2 ± 0.1	29.5 ± 1.6	206.4 ± 21.5	5.41	2.3	8
84671	156681	K4 II	1.2 ± 0.1	53.4 ± 2.7	554.0 ± 54.4	5.03	1.5	5
88048	163917	K0 III	2.7 ± 0.2	14.6 ± 0.3	109.3 ± 3.1	3.32	1.3	10
91004	171115	K3 III	6.4 ± 2.0	. . .	. . .	5.49	1.3	7
100587	194317	K3 III	1.4 ± 0.2	23.6 ± 0.5	159.3 ± 5.4	4.43	1.4	7
114855	219449	K0 III	1.4 ± 0.1	11.0 ± 0.1	51.5 ± 1.1	4.24	1.7	8

Notes. α – HIPPARCOS catalog; β – Reffert et al. (2015); γ – 2MASS catalog.

Thus, we had two options when calibrating our spectra: to use a similar approach to the I_2 cell method using N_2O or NH_3 gas cells (Seifahrt & Käufl 2008; Bean & Seifahrt 2009), or to use atmospheric telluric lines (Huélamo et al. 2008; Figueira et al. 2010). We chose to follow the telluric method.

3.1. Spectral window

Our wavelength setting was selected by inspecting the Arcturus near-IR spectral atlas (Hinkle et al. 1995). We searched for dense stellar line regions that also contained deep and sharp telluric lines to be used for wavelength calibration.

We chose a wavelength setting in the H-band (36/1/n in the CRIRES user manual), with a reference wavelength of λ = 1594.5 nm (wavelength in the middle of detector 3). In fact, the selected region is very close to the wavelength setup successfully used by Figueira et al. (2010). Our setup is characterized by the presence of many sharp atmospheric CO_2 lines, which we used as wavelength calibrators. Unfortunately, the CO_2 lines only fall on detectors 1 and 4. Although detectors 2 and 3 contain many stellar lines, we were not able to construct a wavelength solution for these spectra on these detectors, and thus we excluded detectors 2 and 3 from our analysis.

3.2. Observations

We performed the observations with a standard ABBA nodding cycle, including three jitter observations per nod to subtract the sky background emission. The total exposure time required for each individual target to reach a signal-to-noise ratio $S/N \geq 300$ at the reference wavelength has been estimated with the ESO exposure time calculator[4] (ETC) to be between 18 s for the brightest stars and 3 min for the faintest stars. To achieve the highest possible precision, the spectrograph is used with the 0.2″ slit, resulting in a resolution of R = 100 000. To minimize RV errors related to the imperfect stability of the slit illumination, the

_____

[4] http://etimecalret.eso.org/observing/etc/bin/gen/form?INS.NAME=CRIRES+INS.MODE=swspectr

observations were done in NoAO mode (without adaptive optics), and nights with poor seeing conditions were requested if possible.

Since the periods derived from optical RV data are typically one to two years long, we took at least four RV measurements per year, if possible. During the four semesters of observations some targets were given higher priority than others; the number of data points thus ranges from six to ten.

4. Calibration and data reduction

Dark, flat, and nonlinearity corrections, as well as the combination of raw jittered frames in each nodding position, were performed using the standard ESO CRIRES pipeline recipes. The final output from the CRIRES pipeline is an extracted, one-dimensional coadded spectrum, but we also obtained spectra from the individual A and B nodding frames separately. The CRIRES pipeline wavelength calibration is based on a robust cross-correlation technique between observed spectra and ThAr lamp lines or, alternatively, from a physical model employing ray tracing. However, the precision of both wavelength solutions was insufficient for obtaining precise RVs. We found the wavelength solution from the physical model to be more precise, and thus we used it as an initial guess for the calibration of each spectral frame with telluric lines.

For further data analysis, we developed a semiautomatic pipeline based on a sequence of χ^2 minimization algorithms. Figures 1 and 2 illustrate our data reduction steps on detectors 1 and 4 for the first observation of the K giant HIP 60202.

4.1. Normalization

Continuum normalization of G and K giant spectra is complicated by the high density of spectral lines, which leave almost no continuum level points to work with. To perform a proper continuum normalization, we thus developed an automated algorithm, which identifies areas of the raw spectrum that are free of absorption lines. To find the real continuum points on the raw
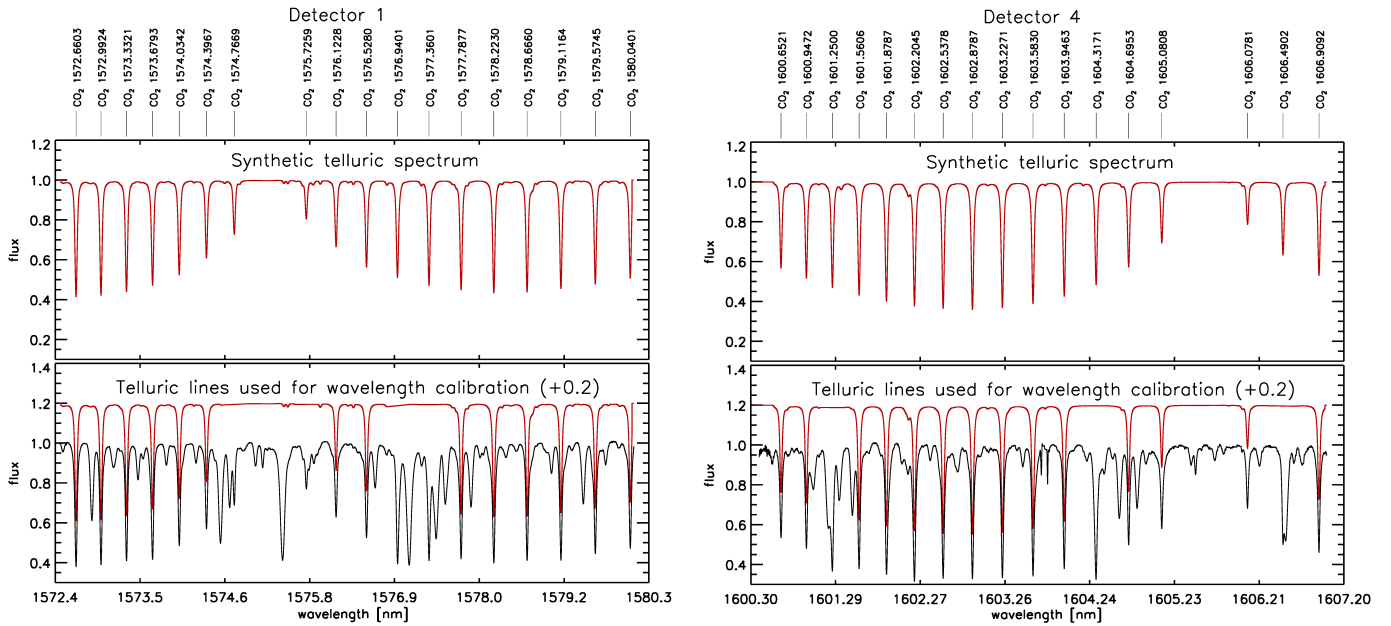
Fig. 1. *Top*: model spectra of the telluric transmission for detectors one (*left*) and four (*right*). *Bottom*: calibrated science spectra for both detectors (black) showing the stellar and telluric absorption lines. Only nonblended telluric lines were modeled (red) and used for constructing the wavelength solution.

spectrum, the same algorithm was applied on a noise-free spectrum constructed by combining a theoretical telluric spectrum and a synthetic stellar spectrum, which was shifted to correct for the barycentric velocity valid for the given epoch of observations (see Sect. 4.2). The matching continuum points between both spectra were selected for the construction of a low-order polynomial fit that represents the estimated continuum level. The raw individual spectrum was then divided by the continuum solution, yielding a normalized spectrum. Extensive testing showed that this algorithm performs a much better continuum normalization in the case of high spectral line densities than the usual algorithm, which assumes that all points below a given threshold belong to the continuum.

4.2. Wavelength calibration

For precise Doppler measurements with CRIRES, a precise wavelength calibration for each epoch and detector must be obtained. We applied several automated steps to first identify all CO_2 lines used for wavelength calibration in the spectra and then to derive their line centroids in pixel and wavelength space.

First we identified all significant absorption lines in the normalized spectrum with relative depths below 0.85 of the continuum level (Pepe et al. 2002). Telluric lines from CO_2 are nearly static, with relatively equidistant wavelengths, and thus were easily identified in the spectra as such. Nevertheless, for precise wavelength calibration on the basis of telluric CO_2 lines, one should take into account that the line centroids may vary depending on the ambient climate above the observatory at the time when the spectrum is obtained. Thus, to assure precise calibration, we adopted methods for telluric spectral synthesis similar to those used in Seifahrt & Käufl (2008), Seifahrt et al. (2010) and Lebzelter et al. (2012).

We used the physical wavelength solution from the CRIRES recipes as initial guess to roughly identify the wavelength region of each observational epoch and for each detector. Next, we constructed a high resolution telluric transmission spectrum

using the Line By Line Radiative Transfer Model[5] (LBLRTM) code for the wavelength region of interest. The precise molecular line positions needed for the model were taken from the HITRAN database (Rothman et al. 1998). For the atmospheric profile above VLT, we adopted the mid-latitude summer/winter meteorological model, which is implemented in the LBLRTM.

Additional input parameters for the atmospheric model included the target's zenith angle as well as ambient atmospheric pressure and temperature at the time of observation. For lack of anything else we used ground-layer pressure and temperature, which might not adequately reflect the conditions higher up in the atmosphere. We were only interested in the CO_2 absorption spectra, but to avoid confusion resulting from any unresolved lines that might appear on science spectra we used all the available atmospheric molecules from HITRAN and obtained the telluric mask. Many other very weak lines caused by other molecules appeared in the theoretical telluric spectra, but they could not be identified separately in the science spectra. Weak molecular lines affect the total continuum level, but apart from that we consider their contribution negligible.

The resulting spectra for detectors one and four were always dominated by many deep and sharp CO_2 lines in absorption. Detector two also showed a few CO_2 absorption lines, but their intensity declined fast toward longer wavelengths and, in general, the lines were heavily blended with stellar lines from the science spectrum. No deep telluric lines could be seen on detector three.

We did not use all of the identified telluric and stellar lines in the following steps. The implemented line identification algorithm effectively excludes lines that are either blended or in close proximity to each other. The selected lines depend on the stellar spectrum shift, which is caused mostly by Earth's barycentric movement. For this reason, a different set of telluric lines was used for wavelength calibration in each observational epoch.

---

[5] LBLRTM – part of FASCODE (Clough et al. 1981, 1992), available at http://rtweb.aer.com/

In the next step, the unblended observed telluric lines in the science spectrum are interpolated and oversampled with a spline function. Line centers are obtained in pixel coordinates by fitting a Gaussian, Lorentzian, or Pseudo-Voigt (weighted sum between a Gaussian and a Lorentzian) profile via χ^2 minimization. The same has been done for the synthetic telluric lines to identify the line centers in wavelength space. Synthetic spectra, by default, are constructed with Voigt profiles, and thus the Voigt profile (approximated as a Pseudo-Voigt profile) is the best choice for fitting. Observed telluric lines are also best represented by Voigt profiles. To avoid possible weak line contamination near the line wings, however, we decided to fit the wavelength range spanning from the line centroid to the line full width at half maximum (FWHM) depth. Many tests showed that at that level the lines are best fit by a Lorentzian profile, and thus we selected the Lorentzian model for telluric fitting instead of the Pseudo-Voigt model.

Finally, the wavelength solution is obtained by constructing a third order polynomial χ^2 fit between the precise CO_2 pixel coordinates of observed telluric lines and their wavelength centers from the synthetic spectra. The wavelength solutions obtained in this way are more precise than those from the CRIRES pipeline and can be used for obtaining precise RVs. Our RV precision, however, will always be limited by the individual telluric lines precision from the HITRAN catalog ($5-50$ m s^{-1}) as well as the telluric variability. The HITRAN catalog precision can in principle be overcome using many lines so that the random errors average out, but the telluric variability is a systematic error that affects all lines in the same way. We tried to limit the random part using as many lines as possible, but blends between atmospheric and stellar lines sometimes did not leave many lines to work with.

4.3. Spectra interpolation and telluric removal

Each wavelength solution for each chip and nodding position was interpolated and resampled onto 10^5 regularly spaced pixels. Based on this oversampled solution, we interpolated the observed and synthetic spectra from their original, irregularly-spaced wavelength solutions onto the regularly spaced pixel grid. The high resolution LBLRTM telluric spectra was interpolated with a sampling factor $L \sim$ three times higher than the original, while the observed spectra have $L \sim 100$ times the number of the original 1024 pixels.

Having both the observed and synthetic telluric spectra on the same wavelength scale is a great advantage. In this way, the telluric lines in both spectra match in wavelength space, which allows us to remove their contribution from each CRIRES spectrum. Synthetic spectra, however, have deeper and narrower lines, and must therefore be smoothed with the CRIRES instrument profile (IP) to match the observed line widths and depths. Instead of measuring each telluric line to identify the IP, we applied a more general strategy. By using a least squares algorithm, we compared the observed spectra, on the one hand, and the synthetic spectra convolved with a Gaussian kernel, on the other hand. An initial guess of the width of the Gaussian kernel is estimated from the spectrograph resolution ($\sim$0.016 nm at $\lambda = 1594.5$ nm); this is the only free parameter in the fit. With this technique, the IP is obtained quickly and independently for each nod and detector. In our test we assumed that the IP is a simple Gaussian, although in reality the IP is a more complicated sum of several Gaussian profiles coming from different optical parts of the spectrograph (Butler et al. 1996; Bean et al. 2010).

Telluric lines may be removed in our pipeline by dividing the observed spectra by the synthetic telluric template convolved with the IP, leaving only the stellar lines. The automated line algorithm was then once again applied to the remaining stellar lines. The laboratory wavelengths of the identified stellar spectral lines were taken from the Vienna Atomic Line Database (VALD, Kupka et al. 1999) and obtained based on the target's $T_{\rm eff}$ and $\log g$. Figure 2 (top panel) illustrates the final output from the spectral division. The figure shows many blended and unblended stellar lines remaining in the spectrum, but there are also many weak stellar lines for which we do not have any information from VALD.

We believe that dividing the spectra in this way provides us with the best stellar template that can be extracted from the CRIRES spectra. This method gives much better results than simply masking the telluric lines from the spectrum. With this approach, we remove the total atmospheric contribution from the science spectra.

5. Obtaining the radial velocities

To derive precise RVs, we adopted a method that combines steps from the least squares modeling as in the iodine method (Butler et al. 1996) and the cross-correlation method (Baranne et al. 1996). Indeed, our wavelength calibrators are atmospheric CO_2 lines, which are always superimposed on the stellar spectra similar to the gas cell method. As we described in Sect. 4, we were able to model the telluric lines and eliminate their contribution from the science spectra. The ideal case would be to use the iodine method to model the telluric and the stellar spectrum simultaneously, where one of the free parameters would be the Doppler shift. In this kind of approach, the blends between telluric and stellar lines would be less problematic. This approach, however, was initially not possible, because we did not have a proper stellar template spectrum in the near-IR region studied. Also, a simultaneous fit would be more complicated in our case because the telluric lines are variable in contrast to the iodine lines, which are stable. Therefore, despite the fact that the four CRIRES detectors cover relatively small spectral regions, our choice was to use a more simplified approach and we obtain RVs by cross-correlating the calibrated spectra with a proper stellar mask.

Initially, when we only had a few CRIRES observations for our targets, we obtained RVs by cross-correlating the stellar spectra with a weighted binary mask (Pepe et al. 2002). Our mask was consistent with noise-free continuum level values at those wavelengths where we did not identify stellar lines and at a noncontinuum level for the stellar wavelength positions. The mask also had adjustable aperture widths to take the stellar line's FWHM into account or to select a pre-defined width, thus making the apertures box-shaped. Even though we achieved relatively good results, we realized that a cross-correlation with weighted binary masks for only a few spectral lines available on each detector might not be optimal. Some near-IR RVs deviated considerably from the Keplerian model prediction, so it became clear that we might be far from the precision goal of $10-25$ m s^{-1}. The main problem was that for some epochs one or even both detectors had only two unblended stellar lines (minimum for our pipeline), which could be used to construct a cross-correlation function (CCF). If one of the two lines is slightly deformed by a nearby line, a delta function or box-like aperture mask also leads to a biased CCF, and consequently to spurious velocity shifts. More lines or an accurate stellar template would mitigate those problems.
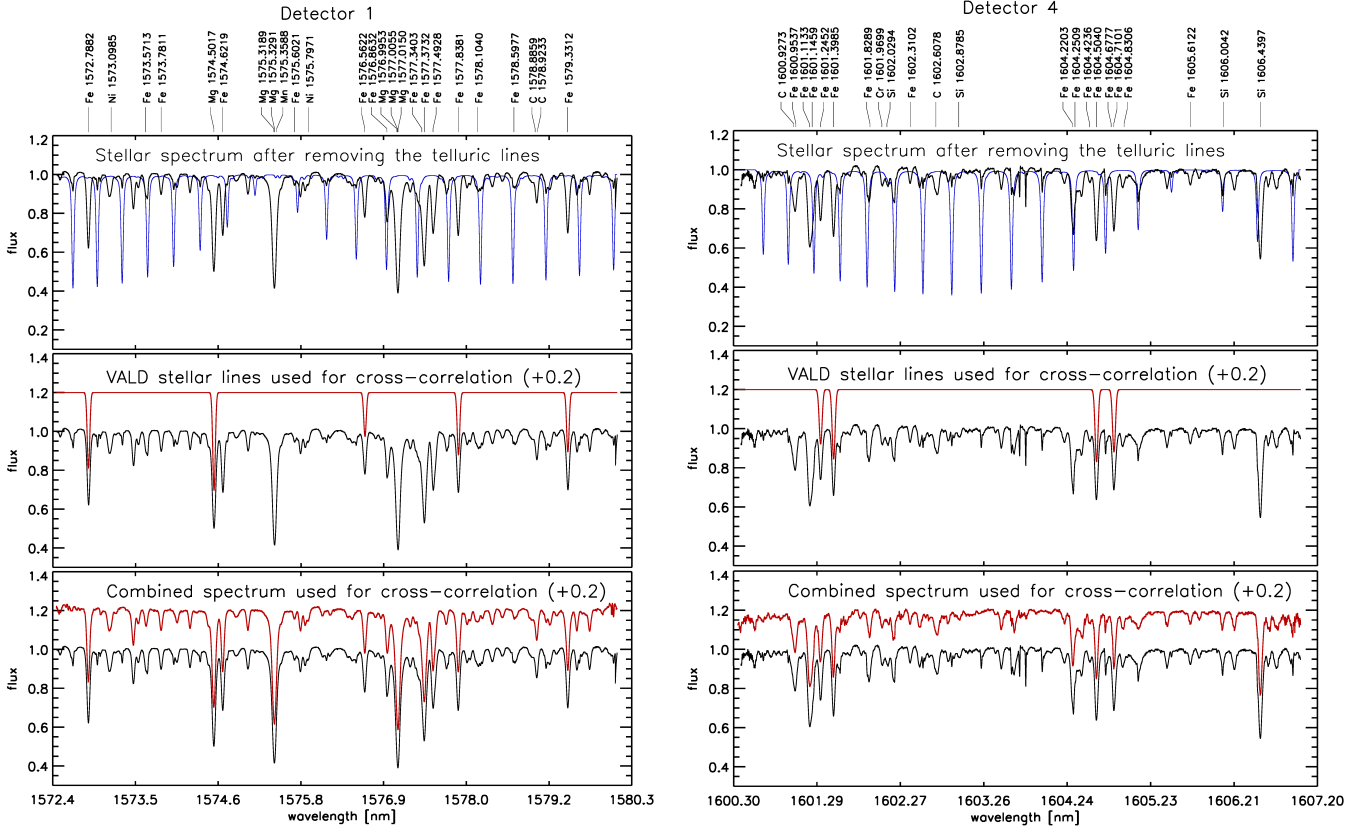
Fig. 2. *Top*: spectra for detector one (*left*) and four (*right*) are divided by the synthetic telluric spectra (blue), removing the atmospheric contribution, and thus only leaving the stellar lines (black). Many of these spectra were automatically identified in the VALD line catalog. *Middle*: only the nonblended lines with well-defined profiles are used for obtaining the RVs via cross-correlation with a synthetic stellar template modeled from the VALD line catalog. *Bottom*: the telluric-free spectra from all observational epochs are later shifted and median-combined in one very high S/N stellar template, which is then used for cross-correlation.

The line position precision, as calculated by state-of-the-art stellar atmosphere models such as PHOENIX[6], is usually worse than that obtained from the high S/N near-IR spectra themselves (Figueira et al. 2010), so we decided to construct an accurate stellar template from our CRIRES observations. The two different ways of constructing the stellar masks are explained below.

5.1. CCF with noise-free stellar mask

To construct a noise-free stellar mask from our observations we chose only single deep and sharp stellar lines (with relative depths below 0.85 of the continuum level, as explained in Sect. 4.2) and modeled these using a Gaussian profile. In fact, initially we did the modeling with Lorentzian and Pseudo-Voigt profiles, but we found that the better fit and lack of complexity of the Gaussian profile suited us well. From this line modeling, we obtained the line FWHM and their individual spectral depths. In the next step, we shifted the identified reference stellar wavelengths by the target's absolute RV[7] and Earth's barycentric motion (accuracy better than ~1 m s^{-1}, Roytman 2013). With this approach, we took all the necessary line shifts into account, so that the synthetic stellar spectrum resulted in line positions very similar to those on the observed stellar spectrum. We thus

constructed a synthetic noise-free stellar spectrum in the same oversampled wavelength space as the observed stellar spectrum.

In Fig. 2 (middle panel) are shown the final stellar masks for detectors one and four. To save computing time, the cross-correlation is calculated for a range of about ±5 km s^{-1} (500 oversampled pixels) around the stellar line centers. The maximum of the CCF can be obtained down to subpixel level using χ^2 minimization; we tried fitting with a Gaussian, a Lorentzian, or a low-order polynomial, which fits a parabola in the area of the maximum of the CCF. Gaussian and Lorentzian models fit the CCF very well, but in contrast to the polynomial model they perform poorly around the CCF peak. The most likely reason for this is that these two models were applied over a wider region of the CCF when compared to the polynomial, which onl fits around the maximum (Allende Prieto 2007). Since we were interested in precisely modeling the peak of the CCF, we selected the polynomial model for deriving precise velocities.

This method of RV computation was applied to the coadded spectra and to the spectra for nodding positions A and B at detectors one and four separately, resulting in six different RVs for a given epoch. The final RV was obtained by calculating a weighted mean of all RVs, where the weight was given by the median S/N of the extracted spectrum, which was taken from the FITS header. Using the S/N for weighting corresponds to the approach used by Butler et al. (1996) for the combination of Doppler information from a large number of short spectral chunks. Usually, the highest S/N ratio was achieved for the

---

coadded spectrum from detector one, and the lowest S/N belonged to one of the nodding positions at detector four.

5.2. CCF with median combined stellar mask

As can be seen from Fig. 2, there are many weak stellar lines on detectors one and four. On top of that there are a few very deep stellar lines that according to the VALD line list are actually spectral doublets. These lines are difficult to model and cannot be used for precise RVs in the context defined in Sect. 5.1.

After the telluric removal on all available spectra, we median combine all frames into another stellar template to be used for cross-correlation. This method has several major advantages:

1. Median combination removes the telluric artifacts still present in the individual frames after the division by the theoretical telluric spectra.
2. All available spectral lines can be used, even unknown lines and unresolved doublet lines. This is not possible by cross-correlating with the noise-free template.
3. Cross-correlation between two identical functions leads to a significant CCF maximum, so that one can very precisely obtain the Doppler shift.

This method, however, requires several challenging steps. Individual spectra have different wavelength shifts and sampling, and thus need to be shifted carefully before median combination. Resampling is done by interpolating each spectrum to the most precise wavelength solution achieved so far (i.e., most telluric references have been used). Each spectrum is then shifted exactly by the difference to the reference spectrum and, finally, a median combination is applied. The result is a high S/N stellar mask with the most precise wavelength solution for a given target.

This method was only applicable after we had acquired 5−8 epochs for each target. The final median combined stellar template spectrum for each target on detector one and four is shown in Figs. A.1 and A.2. The RVs seem to be more precise from detector one than from detector four, where the lower S/N and the abundant and faint stellar lines influence the CCF.

The resulting RV for each epoch is obtained with the same cross-correlation steps and weighted combination of individual frame RVs as explained in Sect. 5.1 for the noise-free stellar template. The measured near-infrared RVs for all stars using this method are listed in Table A.1.

5.3. Error estimation

The RV uncertainties depend on the number of telluric lines used for the calibration (i.e., the reproducibility of the wavelength solution), the lines used for cross-correlation, and the stellar flux from each individual star. We did not assess these systematic errors quantitatively nor did we consider the HITRAN and VALD line errors individually. Instead, for each observation we used one combined error, which is based on the RV dispersion from all nodding and coadded positions. The RV error computed in this way varies greatly from epoch to epoch, with a mean value of about ∼25 m s^{-1}. The individual error for each observation is listed in Table A.1.

Based on our results, we estimated the total error of our CRIRES measurements to be not more than 40 m s^{-1}. This estimation was further confirmed by the total rms dispersion of the near-IR velocities around the best-fit model obtained for each target from the Lick velocities.

6. IR radial velocity analysis

6.1. Consistency between optical and IR data

Eight stars in our sample have published planetary companions, including two two-planet systems. For those ten planets[8] the five spectroscopic orbital parameters characterizing a Keplerian orbit are known rather accurately. To test whether the CRIRES RVs support the planet hypothesis, we fitted Keplerian orbits to the CRIRES RVs for each star as well. However, since we have far fewer data points from CRIRES than in the optical, sometimes with incomplete phase coverage, we only fit for the RV semiamplitude as well as the RV zero point; we also keep the other four spectroscopic parameters (period, periastron time, eccentricity, and longitude of periastron) fixed at the values derived from the optical RVs. We note that our observations with CRIRES were scheduled to sample the RV signal as well as possible in phase over the orbital period. With this approach, we tried to avoid uneven sampling of the data because it can lead to possible zero velocity crossings and a poorly resolved periastron passage (e.g., Cumming 2004), which can lead to highly uncertain amplitude ratios.

For the two stars with two planets, the fitting was done one planet at a time, while the RV signal of the other planet as determined from the optical data was subtracted. This approach assumes that the RV signal of the subtracted planet is consistent in the optical and the IR; when this is not the case then this inconsistency would show up in the comparison of the RV signals for the other planet in the system.

As in the optical, we quadratically added an RV jitter term to the RV measurement errors to account for stellar noise (pulsations). We did not make any attempt to derive a different value for the jitter term from the CRIRES data, but used the jitter term derived from the optical data. For the eight stars investigated here, the RV jitter term varies from about a third of the value of the IR RV measurement error up to about twice its value.

The resulting RV semiamplitudes in the optical ($K_{\rm opt}$) and in the IR ($K_{\rm IR}$) are given in Table 2 together with their errors derived from χ^2 fitting. Table 2 also shows the rms values of the optical and IR data from the best optical and IR models, respectively. The last column in the table gives the proportion κ between those two RV amplitudes: $\kappa = K_{\rm IR}/K_{\rm opt}$, along with its error derived following simple error propagation. The RV semiamplitudes $K_{\rm opt}$ and $K_{\rm IR}$ are also shown in Fig. 3. The solid line corresponds to $\kappa = 1$, i.e., the same RV semiamplitude in both wavelength regimes. In Fig. 4, the resulting Keplerian RV curves for the optical and the IR wavelength regime are shown together with the CRIRES measurements.

The RV semiamplitude of the outer planet in the HIP 88048 system is not constrained by the CRIRES data, which leaves nine planets in eight systems for our analysis. As one can see, the optical and the IR data are consistent (i.e., $\kappa \approx 1$) at the $1−1.5\sigma$ level for all nine investigated planets.

In the case of a RV signal, which is at least partly due to stellar noise (starspots, pulsations, etc.), one might expect different RV amplitudes or phases in the optical and in the infrared since the contrast between the various regions on the stellar surface is wavelength dependent. The agreement between optical and infrared amplitude further supports the planetary hypothesis in all eight systems, as expected further tests might be required to undoubtedly confirm the planet interpretation. We will discuss the other systems individually in forthcoming papers.

---

[8] For simplicity we also use the term planet for deuterium burning mass objects (brown dwarf) as defined in Reffert et al. (2015).

Table 2. Comparison of best optical (K_{opt}) and IR (K_{IR}) RV semiamplitudes and companion between the optical and IR data rms values from these models.

HIP	K_{opt} [m s^{-1}]	rms$_{opt}$ [m s^{-1}]	K_{IR} [m s^{-1}]	rms$_{IR}$ [m s^{-1}]	$\kappa = K_{IR}/K_{opt}$	Reference
5364 b	51.1 ± 2.5	16.3	65.7 ± 14.6	23.3	1.29 ± 0.29	Trifonov et al. (2014)
5364 c	52.9 ± 2.6	16.3	71.5 ± 17.9	26.7	1.35 ± 0.35	Trifonov et al. (2014)
20889 b	93.2 ± 2.1	10.7	89.5 ± 8.3	44.1	0.96 ± 0.09	Sato et al. (2007)
31592 b	45.2 ± 4.7	7.3	47.0 ± 10.8	31.8	1.04 ± 0.24	Wittenmyer et al. (2011)
34693 b	350.5 ± 3.4	21.1	326.2 ± 13.6	39.9	0.93 ± 0.04	Mitchell et al. (2013)
37826 b	46.0 ± 1.6	10.9	70.1 ± 12.6	15.4	1.52 ± 0.27	Reffert et al. (2006)
60202 b	296.7 ± 5.6	30.0	277.8 ± 26.1	55.9	0.94 ± 0.09	Liu et al. (2008)
88048 b	288.4 ± 1.2	9.0	253.4 ± 23.1	20.9	0.88 ± 0.08	Quirrenbach et al. (2011)
88048 c	175.2 ± 1.4	9.0	…	…	…	Quirrenbach et al. (2011)
114855 b	91.0 ± 2.3	18.9	120.7 ± 24.3	39.8	1.33 ± 0.27	Mitchell et al. (2013)

Notes. The sixth column gives the proportion between the two semiamplitudes.

6.2. IR data phase coverage

Given the relatively sparse IR data sampling for our targets as well as the moderately large IR RV errors, we investigated whether this might lead to systematic errors in the fitted RV semiamplitudes. We simulated 10 000 alternative IR data sets for each of the eight stars. We assumed the optical orbit to be the correct data set and we randomly simulated IR data drawn from a normal distribution around the best optical fit, but at the same observational times and with errors as in our original CRIRES measurements. For each simulated data set, we fitted the RV semiamplitude as described in Sect. 6.1, keeping the rest of the orbital parameters fixed at the optical solution. The resulting distribution of RV semiamplitudes was fitted with a Gaussian, from which we obtained the mean RV semiamplitude and its standard deviation. This test should tell us whether the incomplete phase coverage coupled with the relatively large IR RV errors would lead to any systematics in the recovered RV semiamplitudes.

We found that for all targets listed in Table 2 the RV semiamplitude could be recovered from the simulated data without any systematic offsets. The biggest difference we found between the optical and the simulated RV semiamplitude was ~0.3 m s^{-1}, which is completely insignificant. We conclude that there are no systematic differences in κ due to the sparse sampling and large error of the IR data set.

7. Discussion

7.1. RV precision

As discussed in Sect. 5.3, the RV precision achieved with CRIRES spectra depends strongly on the number of telluric and stellar lines used for wavelength calibration and cross-correlation, respectively. In this context we find that giants of spectral type G8 III – K2 III are the best targets from our CRIRES survey in terms of RV precision, when we cross-correlate with the noise-free stellar mask (see Sect. 5.1). These stars have a small number of deep stellar lines, and hence, the problematic line contamination with CO_2 lines is minimized. We were able to use a maximum number of telluric lines for precise wavelength calibration and almost in any epoch we had enough unblended stellar lines to obtain RVs. We achieved similar results for these stars when we cross-correlate the telluric free spectra with the median-combined stellar mask (see Sect. 5.2). For G8 III – K2 III giants we achieved an overall mean RV precision of about 25 m s^{-1}. Also, it is worth mentioning that

G8 III – K2 III giants have in general lower levels of stellar RV jitter than later K giants, and the velocity precision achieved was adequate to test the near-IR velocities for agreement with optical data, and hence, to test for the presence of a planetary companion.

Although both methods worked well for G8 III – K2 III giants, the noise-free mask failed to give reasonable velocities for K3 III – K4 III giants. The reason for that is the abundance of stellar lines typical for late K stars (see Figs. A.1 and A.2). Heavy line blending mutually excluded large number of lines usable for the wavelength solution and cross-correlation. We find that for many cases in given epochs the RV dispersion between the individual detector nods is too large to derive an adequate RV precision. Unlike the noise-free stellar mask, the median mask is less sensitive to blended stellar lines (since we use all available stellar lines to construct the CCF) and generally gave better results for these stars. Although in some cases the low number of unblended telluric lines was still a problem for constructing a precise wavelength solution, the full set of stellar lines used in this method led to a significant CCF peak from which we could obtain the RVs with a decent precision. The only way to obtain reasonable RVs for K3 III – K4 III giants was with the median stellar template. Using this method, we achieved mean precision of 20 m s^{-1}, which is even slightly better than that for G8 III – K2 III.

7.2. Substellar companions

Lick and CRIRES data for HIP 114855 and HIP 34693 have already been published in Mitchell et al. (2013), while the multiple planetary system around HIP 5364 was extensively discussed in Trifonov et al. (2014). Here we present improved CRIRES velocities for these targets based on cross-correlation with the median-combined mask, superceding earlier results. Results from our near-IR study based on the new CRIRES velocities for these stars are given in Table 2 and Fig. 4. All three stars have consistent optical and near-IR semiamplitudes at the 1−1.5σ level. The relatively sparse near-IR sample for HIP 114855 and HIP 34693 has excellent phase coverage showing consistency with the best optical Keplerian model. HIP 5364 has a rather good near-IR phase coverage with data mostly sampled around the two-planet signal extrema, but more near-IR RVs for later epochs would be highly desirable. As was demonstrated in Trifonov et al. (2014), Lick and CRIRES data are more consistent with a two-planet dynamical model rather than a simple double Keplerian model, and thus strongly argue
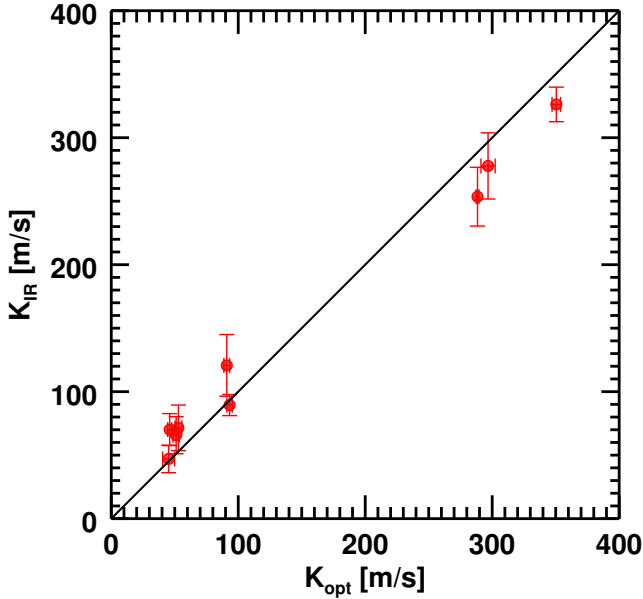
Fig. 3. Comparison of the optical (K_{opt}) and infrared (K_{IR}) RV semi-amplitudes. The straight line corresponds to $K_{opt} = K_{IR}$. Overall we observe a good correspondence between K_{opt} and K_{IR}; the largest deviations are at the 1.5σ level.

for the presence of gravitationally interacting planets. However, for longer time spans the difference between the Keplerian and the dynamical model is much larger, and thus more data certainly helps to reveal HIP 5364 system's architecture in more detail. We conclude that HIP 114855, HIP 34693, and HIP 5364 have secure planets.

HIP 60202 has a substellar companion with minimum mass in the brown dwarf regime ($m_b \sin i \approx 17\ M_{Jup}$), first reported in Liu et al. (2008). More optical velocities from Lick for this star will be published in Mitchell et al. (in prep.). Our CRIRES velocities for this star are consistent with the Keplerian model based on the combined optical velocities from Lick and those published in Liu et al. (2008). We found that compared to the optical model the near-IR data favor a slightly smaller RV semi-amplitude ($\kappa = 0.94 \pm 0.09$), but both data sets are clearly consistent with each other. As can be seen in Fig. 4, the sparse near-IR data set does not cover the time of the predicted RV minimum, which is most likely the reason for the lower κ. We conclude that the IR data support an orbiting companion around HIP 60202.

The optical Doppler velocities for the K0 III giant HIP 88048 are clearly consistent with two massive companions on noncircular orbits. Based on our Lick data, two brown dwarf companions were first discovered by Quirrenbach et al. (2011) and later confirmed by Sato et al. (2012). The Keplerian nature of the optical velocity data was generally accepted, since other phenomena intrinsic to the star are very unlikely to be responsible for the Doppler signal. The period of the outer companion exceeds several times the time span of the CRIRES observations, and thus at this stage we cannot derive any κ value for the second RV signal. The near-IR data cover only about one full period of the inner planet and clearly follow the optical model, but with poor phase coverage at the predicted RV maximum (see Fig. 4). Our semi-amplitude analysis resulted in $\kappa = 0.88 \pm 0.08$, which is about 1.5σ from the best optical fit.

We also confirm the presence of planetary companions around HIP 20889 (Sato et al. 2007) and HIP 37826 (Reffert et al. 2006; Hatzes et al. 2006). For HIP 20889, the near-IR data cover one full period and the velocity amplitude fully agrees with

the amplitude from the optical resulting in $\kappa = 0.96 \pm 0.09$. For HIP 37826, the near-IR velocity amplitude is larger than the predicted amplitude with $\kappa = 1.52 \pm 0.27$, but the near-IR value is still within 2σ from the best optical semi-amplitude. The reason for the larger κ is most likely the relatively large near-IR RV errors compared to the optical semi-amplitude for HIP 37826. Another complication might be the phase coverage; there are several measurements around the minimum and maximum RV, but in between there is a gap. The CRIRES data follow the Keplerian predictions for these stars; the near-IR RV signal has slightly larger velocity dispersion than the optical data, as expected.

The CRIRES data are best suited for testing RV models that assume brown dwarf mass objects in orbit (HIP 34693, HIP 60202 and HIP 88048), since these stars have large RV semiamplitudes and the CRIRES RV uncertainties are still adequate to detect the periodic RV signal. It was more challenging for planetary mass objects, since their RV semiamplitude was usually only between two and four times of the achieved CRIRES measurement precision. This was the case for HIP 31592, where the optical semiamplitude is on the order of ~ 45 m s^{-1} and it is on the same order with some of the obtained errors from CRIRES (see Fig. 4). Despite the large errors, however, the near-IR data for HIP 31592 are consistent and are best fitted with an amplitude that is about the same as in the optical ($\kappa = 1.04 \pm 0.24$). These results imply that the planet announced in Wittenmyer et al. (2011) is very likely real, although this star will benefit from more precise RV data with better phase coverage.

8. Summary

The main goal of our study was to confirm or disprove the planetary origin of radial-velocity variations observed in G and K giants. For this purpose, we compared a set of high precision optical and near-IR RVs and searched for consistency between the two wavelength domains.

For our test we selected 20 G and K giants that we extensively observed for more than a decade at Lick observatory and that all show periodicity in the optical RV data. For some of the stars orbiting planets have been announced or will be published in the future, and for some there are indications (from the optical data alone) that the RV periodicity might also be caused by stellar activity. For all stars however the RV signal is very persistent, so that we were able to fit Keplerian orbits consistent with one or two orbiting substellar companions.

We obtained precise near-IR RVs with ESO's CRIRES spectrograph for these stars and in this paper we presented our observational setup, data reduction strategy, and results. We selected a spectral region in the H-band, which is known to have abundant atmospheric CO_2 lines that we used for wavelength calibration. Only detectors one and four were used for our analysis.

To achieve a precise wavelength solution, we adopted the CO_2 line centroids from a synthetic telluric spectrum constructed from a line-by-line radiative transfer code (LBLRTM), which uses as an input the HITRAN atmospheric line catalog and the ambient conditions at the time of the observations. By performing a division between the synthetic atmospheric spectrum and the science spectrum, we precisely removed the telluric line contamination, leaving only the stellar lines.

Finally, we derived the RVs by cross-correlating the observed spectra with noise-free stellar masks constructed from the VALD theoretical wavelengths and the modeled nonblended stellar line profiles from the observed spectra. This method
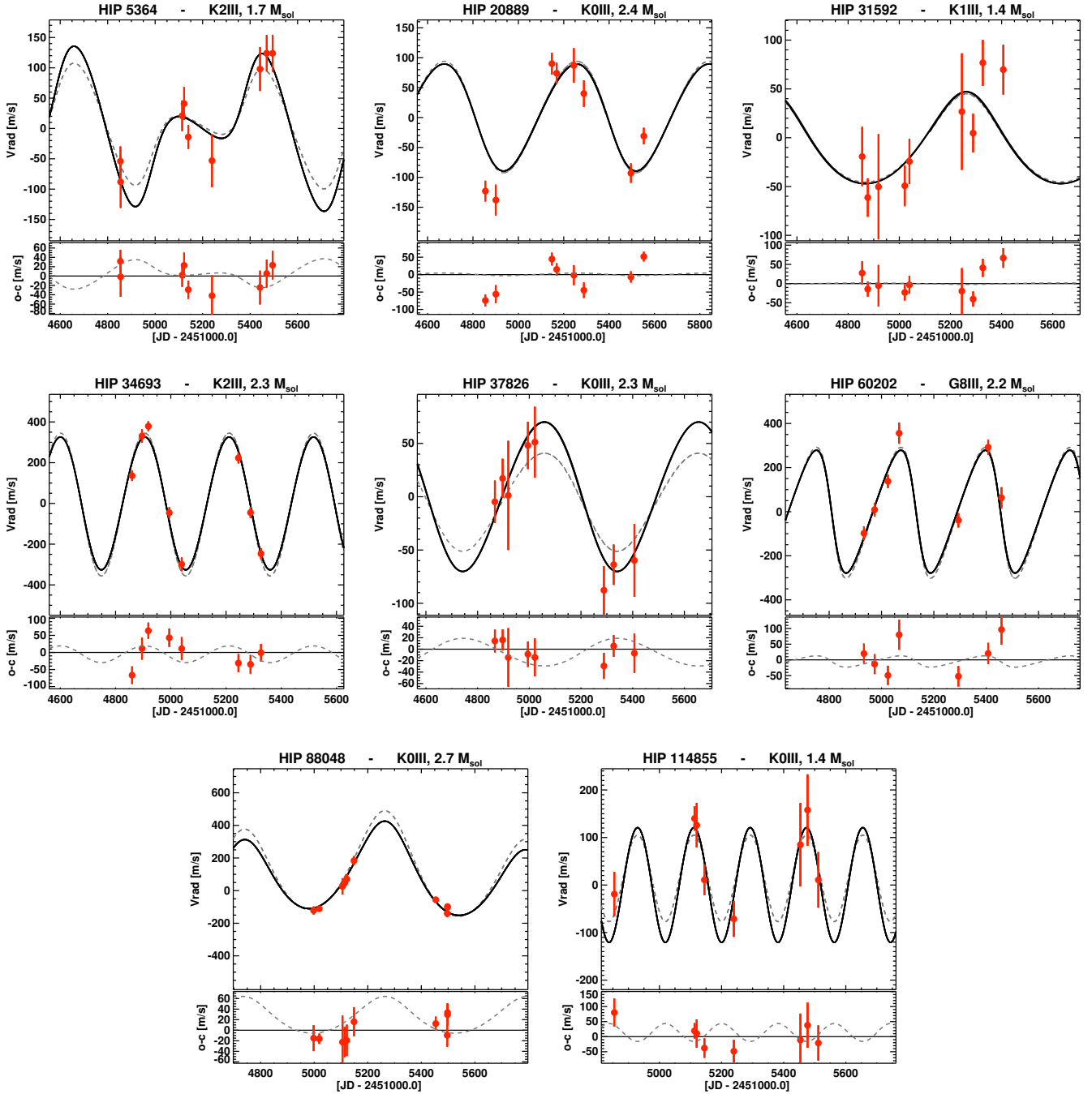
Fig. 4. CRIRES near-IR RVs for the targets known to have planetary companions. Two best fits to the CRIRES data are overplotted: the model for the best-fit value of κ, where K_{IR} is a free parameter is plotted with a solid black line, while the gray dashed line is for $\kappa = 1$, which is the best Keplerian model obtained from the literature data (optical). *Bottom panels* show the residuals around the best-fit value of κ. The dashed line in the residual panel illustrates the difference between the two models.

worked well for G8 III – K1 III and some K2 III giants, but failed to give reasonable velocities for later K giants. Therefore, once we had enough observational epochs for each target we combined all available target spectra into a master template. We cross-correlated this high S/N stellar template with each observed spectrum to extract the maximum Doppler information from all stellar lines in the spectra. This improved strategy gave excellent results for almost all spectral types in our sample, including the late K giants.

The RV precision varies considerably from epoch to epoch and from star to star; the mean RV error is about 25 m s^{-1}. The

achieved RV precision was adequate to address our scientific question only for the stars with larger RV amplitudes.

The near-IR RVs are in general in excellent agreement with the optical data; we did not find a single system where the two data sets are inconsistent with each other. For a small number of stars the interpretation is unclear, since we would need more precise data to perform the comparison. For all eight stars that we investigated in detail, the derived near-IR RVs agree well with the Lick data. They follow the best Keplerian model predictions and in particular they are consistent in amplitude, so that we confirm the planets in the following systems (cf. Table 2): HIP 5364

(η Cet), HIP 20889 (ϵ Tau), HIP 31592 (7 CMa), HIP 34693 (τ Gem), HIP 37826 (β Gem), HIP 60202 (11 Com), HIP 88048 (ν Oph) and HIP 114855 (91 Aqr). We conclude that the vast majority of the planetary systems known or suspected to exist around the massive evolved stars from our sample is most likely real.

References

Allende Prieto, C. 2007, AJ, 134, 1843
Baranne, A., Queloz, D., Mayor, M., et al. 1996, A&AS, 119, 373
Barban, C., De Ridder, J., Mazumdar, A., et al. 2004, in SOHO 14 Helio- and Asteroseismology: Towards a Golden Future, ed. D. Danesy, ESA SP, 559, 113
Bean, J. L., & Seifahrt, A. 2009, A&A, 496, 249
Bean, J. L., Seifahrt, A., Hartman, H., et al. 2010, ApJ, 713, 410
Butler, R. P., Marcy, G. W., Williams, E., et al. 1996, PASP, 108, 500
Clough, S. A., Kneizys, F. X., Rothman, L. S., & Gallery, W. O. 1981, in Atmospheric transmission, SPIE Conf. Ser., 277, 152
Clough, S. A., Iacono, M. J., & Moncet, J.-L. 1992, J. Geophys. Res., 97, 15761
Cumming, A. 2004, MNRAS, 354, 1165
Desort, M., Lagrange, A.-M., Galland, F., Udry, S., & Mayor, M. 2007, A&A, 473, 983
Dorn, R. J., Anglada-Escude, G., Baade, D., et al. 2014, The Messenger, 156, 7
Figueira, P., Pepe, F., Melo, C. H. F., et al. 2010, A&A, 511, A55
Frink, S., Quirrenbach, A., Fischer, D., Röser, S., & Schilbach, E. 2001, PASP, 113, 173
Frink, S., Mitchell, D. S., Quirrenbach, A., et al. 2002, ApJ, 576, 478
Hatzes, A. P. 2002, Astron. Nachr., 323, 392
Hatzes, A. P., & Cochran, W. D. 2000, AJ, 120, 979
Hatzes, A. P., Cochran, W. D., Endl, M., et al. 2006, A&A, 457, 335
Hinkle, K., Wallace, L., & Livingston, W. 1995, PASP, 107, 1042
Huélamo, N., Figueira, P., Bonfils, X., et al. 2008, A&A, 489, L9
Kaeufl, H.-U., Ballester, P., Biereichel, P., et al. 2004, in SPIE Conf. Ser. 5492, eds. A. F. M. Moorwood, & M. Iye, 1218
Kupka, F., Piskunov, N., Ryabchikova, T. A., Stempels, H. C., & Weiss, W. W. 1999, A&AS, 138, 119
Lebzelter, T., Seifahrt, A., Uttenthaler, S., et al. 2012, A&A, 539, A109
Liu, Y.-J., Sato, B., Zhao, G., et al. 2008, ApJ, 672, 553
Marcy, G. W., & Butler, R. P. 1992, PASP, 104, 270
Mayor, M., Pepe, F., Queloz, D., et al. 2003, The Messenger, 114, 20
Mitchell, D. S., Reffert, S., Trifonov, T., Quirrenbach, A., & Fischer, D. A. 2013, A&A, 555, A87
Moutou, C., Mayor, M., Lo Curto, G., et al. 2011, A&A, 527, A63
Pepe, F., Mayor, M., Galland, F., et al. 2002, A&A, 388, 632
Quirrenbach, A., Reffert, S., & Bergmann, C. 2011, in AIP Conf. Ser. 1331, eds. S. Schuh, H. Drechsel, & U. Heber, 102
Reffert, S., Quirrenbach, A., Mitchell, D. S., et al. 2006, ApJ, 652, 661
Reffert, S., Bergmann, C., Quirrenbach, A., Trifonov, T., & Künstler, A. 2015, A&A, 574, A116
Reiners, A., Bean, J. L., Huber, K. F., et al. 2010, ApJ, 710, 432
Rothman, L. S., Rinsland, C. P., Goldman, A., et al. 1998, J. Quant. Spectr. Rad. Transf., 60, 665
Roytman, N. 2013, Diplomarbeit, Landessternwarte, Heidelberg University, Germany
Sato, B., Izumiura, H., Toyota, E., et al. 2007, ApJ, 661, 527
Sato, B., Omiya, M., Harakawa, H., et al. 2012, PASJ, 64, 135
Sato, B., Omiya, M., Harakawa, H., et al. 2013, PASJ, 65, 85
Seifahrt, A., & Käufl, H. U. 2008, A&A, 491, 929
Seifahrt, A., Käufl, H. U., Zängl, G., et al. 2010, A&A, 524, A11
Setiawan, J., Henning, T., Launhardt, R., et al. 2008, Nature, 451, 38
Trifonov, T., Reffert, S., Tan, X., Lee, M. H., & Quirrenbach, A. 2014, A&A, 568, A64
Wittenmyer, R. A., Endl, M., Wang, L., et al. 2011, ApJ, 743, 184
Zechmeister, M., Reffert, S., Hatzes, A. P., Endl, M., & Quirrenbach, A. 2008, A&A, 491, 531

Appendix A

Table A.1. Radial velocities measured with CRIRES.

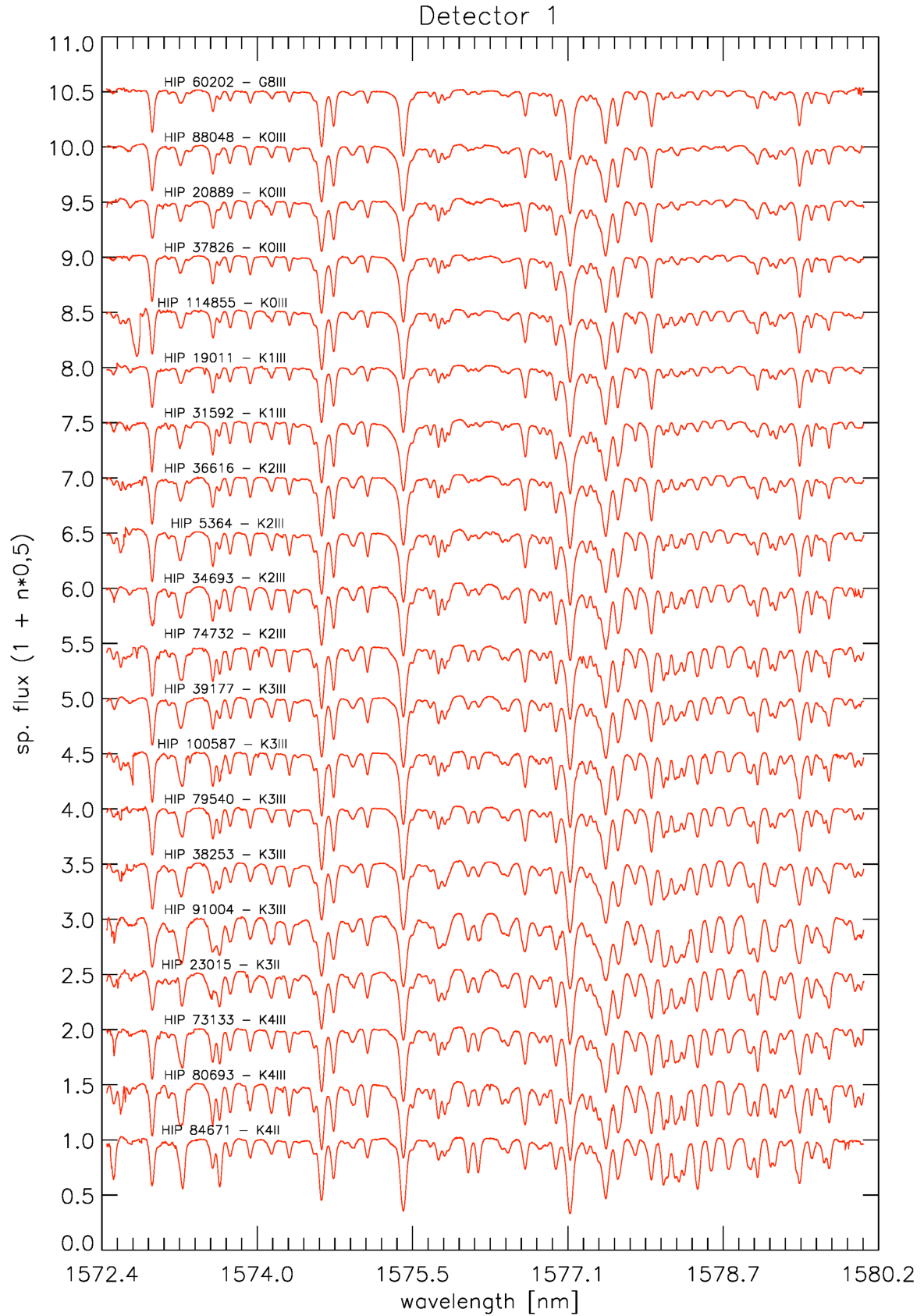| Target	Epoch [JD]	RV [km s⁻¹]	σ [m s⁻¹]	Target	Epoch [JD]	RV [km s⁻¹]	σ [m s⁻¹]	Target	Epoch [JD]	RV [km s⁻¹]	σ [m s⁻¹]
HIP 5364	2 455 853.844	11.623	19		2 456 288.592	−34.193	29		2 456 453.802	−23.342	15
	2 455 854.616	11.588	40		2 456 326.559	−34.333	55		2 456 496.664	−23.374	17
	2 456 113.863	11.697	20		2 456 406.504	−34.328	47		2 456 503.652	−23.376	9
	2 456 121.811	11.717	22	HIP 37826	2 455 866.855	3.706	17	HIP 80693	2 455 990.888	7.561	13
	2 456 139.747	11.662	12		2 455 896.833	3.728	15		2 456 015.773	7.956	11
	2 456 239.563	11.623	41		2 455 918.718	3.712	50		2 456 025.680	7.820	21
	2 456 441.910	11.774	33		2 455 994.554	3.759	19		2 456 025.676	7.832	24
	2 456 469.917	11.801	26		2 456 021.584	3.762	31		2 456 121.559	7.813	50
	2 456 494.892	11.800	26		2 456 288.709	3.623	20		2 456 406.714	7.826	13
HIP 19011	2 455 854.736	26.864	6		2 456 326.567	3.647	15		2 456 459.675	7.956	19
	2 455 876.638	26.854	8		2 456 406.514	3.651	32		2 456 511.625	8.063	9
	2 456 141.856	27.007	5	HIP 38253	2 455 859.837	−3.777	9	HIP 84671	2 455 994.793	38.930	8
	2 456 147.907	27.020	7		2 455 896.774	−3.822	20		2 456 018.858	39.056	10
	2 456 244.602	26.923	12		2 455 918.723	−3.840	24		2 456 105.639	39.164	50
	2 456 287.561	26.917	23		2 455 973.736	−4.039	17		2 456 121.670	39.315	145
HIP 20889	2 455 854.744	38.407	14		2 456 021.597	−3.936	21		2 456 148.674	39.137	21
	2 455 900.760	38.392	24		2 456 244.742	−4.311	12	HIP 88048	2 455 997.887	12.901	23
	2 456 147.921	38.620	15		2 456 288.586	−3.759	18		2 456 018.852	12.912	6
	2 456 168.832	38.604	14		2 456 326.571	−3.851	8		2 456 105.635	13.048	49
	2 456 244.649	38.618	27	HIP 39177	2 455 859.843	39.473	13		2 456 113.599	13.068	28
	2 456 288.569	38.571	20		2 455 896.768	39.511	5		2 456 121.780	13.093	29
	2 456 495.931	38.438	13		2 455 918.731	39.502	7		2 456 148.679	13.206	26
	2 456 552.779	38.499	9		2 455 973.728	39.390	9		2 456 453.870	12.966	11
HIP 23015	2 455 854.777	16.997	9		2 456 021.589	39.500	13		2 456 496.673	12.882	20
	2 455 900.755	16.728	7		2 456 288.701	39.254	8		2 456 497.759	12.925	16
	2 456 168.898	17.143	17		2 456 326.578	39.264	4		2 456 497.767	12.920	19
	2 456 169.900	17.222	31	HIP 60202	2 455 932.826	43.196	10	HIP 91004	2 455 855.571	−3.084	28
	2 456 244.738	16.933	16		2 455 973.744	43.302	10		2 455 997.891	−3.574	9
	2 456 288.574	16.320	17		2 456 024.594	43.431	6		2 456 114.775	−3.654	3
HIP 31592	2 455 854.862	2.606	29		2 456 067.482	43.650	37		2 456 119.832	−3.580	41
	2 455 876.701	2.564	18		2 456 293.849	43.255	13		2 456 119.846	−3.538	23
	2 455 918.706	2.575	53		2 456 407.498	43.586	15		2 456 141.792	−3.416	25
	2 456 021.552	2.576	19		2 456 458.561	43.356	37		2 456 239.543	−2.432	4
	2 456 039.484	2.601	22	HIP 73133	2 455 937.846	17.637	6	HIP 100587	2 455 860.541	−15.468	4
	2 456 244.653	2.652	59		2 455 994.777	17.749	12		2 456 113.859	−15.268	6
	2 456 288.579	2.630	18		2 456 022.713	17.744	15		2 456 119.838	−15.278	11
	2 456 326.544	2.702	22		2 456 067.488	17.808	11		2 456 144.750	−15.207	50
	2 456 406.497	2.695	24		2 456 406.698	18.099	34		2 456 405.903	−14.705	11
HIP 34693	2 455 859.855	22.027	11		2 456 458.572	18.196	13		2 456 440.905	−14.680	20
	2 455 895.863	22.222	23	HIP 74732	2 455 939.840	−9.514	10		2 456 466.747	−14.607	37
	2 455 918.699	22.270	6		2 455 994.784	−9.493	13	HIP 114855	2 455 854.611	−25.721	43
	2 455 994.537	21.845	14		2 456 024.647	−9.526	6		2 456 112.928	−25.563	17
	2 456 039.510	21.592	25		2 456 067.495	−9.601	9		2 456 119.880	−25.576	43
	2 456 244.866	22.114	13		2 456 406.729	−9.466	10		2 456 144.774	−25.691	26
	2 456 288.696	21.846	14		2 456 453.796	−9.350	13		2 456 239.555	−25.773	33
	2 456 326.553	21.644	12		2 456 494.649	−9.323	18		2 456 453.898	−25.617	86
HIP 36616	2 455 859.849	−35.057	17	HIP 79540	2 456 015.780	−23.336	14		2 456 476.910	−25.545	73
	2 455 896.842	−34.848	72		2 456 105.644	−23.399	22		2 456 511.637	−25.691	55
	2 455 918.683	−34.780	33		2 456 113.594	−23.406	18				
	2 455 994.545	−34.800	18		2 456 121.644	−23.459	25				
	2 456 021.576	−34.910	49		2 456 406.706	−23.391	22				

Fig. A.1. Median-combined spectra from detector 1 for all observed targets, shifted by +0.5 in ascending order starting from K4 III giants at the bottom to earlier spectral type stars toward the top. Telluric lines were removed. Obviously late G and early K giants have a smaller number of deep stellar lines in this wavelength region than later K giants.
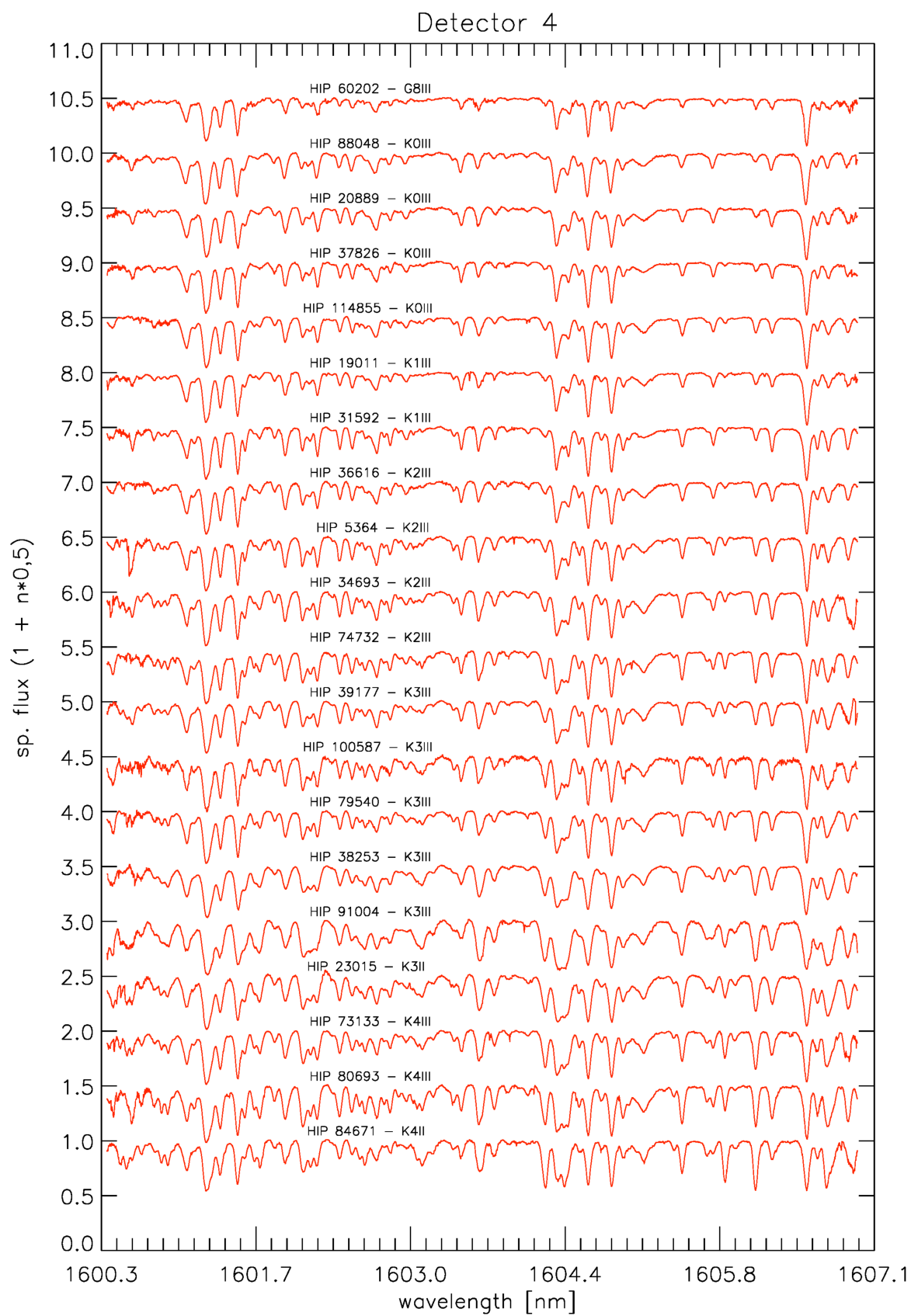
Fig. A.2. Same as Fig. A.1, except for detector 4. Detector 4 has in general lower S/N when compared to detector 1.